

Circulation and dissipation on hot Jupiters

J. Li and J. Goodman

Princeton University Observatory, Princeton, NJ 08544

jeremy@astro.princeton.edu

ABSTRACT

Many global circulation models predict supersonic zonal winds and large vertical shears in the atmospheres of short-period jovian exoplanets. Using linear analysis and nonlinear local simulations, we investigate hydrodynamic dissipation mechanisms to balance the thermal acceleration of these winds. The adiabatic Richardson criterion remains a good guide to linear stability, although thermal diffusion allows some modes to violate it at very long wavelengths and very low growth rates. Nonlinearly, wind speeds saturate at Mach numbers ≈ 2 and Richardson numbers $\lesssim 1/4$ for a broad range of plausible diffusivities and forcing strengths. Turbulence and vertical mixing, though accompanied by weak shocks, dominate the dissipation, which appears to be the outcome of a recurrent Kelvin-Helmholtz instability. An explicit shear viscosity, as well as thermal diffusivity, is added to ZEUS to capture dissipation outside of shocks. The wind speed is not monotonic nor single valued for shear viscosities larger than about 10^{-3} of the sound speed times the pressure scale height. Coarsening the numerical resolution can also increase the speed. Hence global simulations that are incapable of representing vertical turbulence and shocks, either because of reduced physics or because of limited resolution, may overestimate wind speeds. We recommend that such simulations include artificial dissipation terms to control the Mach and Richardson numbers and to capture mechanical dissipation as heat.

Subject headings: binaries: close—hydrodynamics—instabilities—planetary systems—shock waves—turbulence

1. Introduction

Strongly irradiated extrasolar giant planets—“hot Jupiters”—are expected to rotate synchronously with their orbits but to have strong longitudinal winds that redistribute heat

from the day to the night side. The efficiency of redistribution is important for direct observables including infrared phase curves, the depth of secondary eclipses in transiting systems (i.e., eclipses of the planet by its star), and planetary spectra. Turbulence associated with the winds may contribute to chemical mixing of the atmosphere (Spiegel et al. 2009), and might even inject heat into the convective interior of the planet (Guillot & Showman 2002), thereby perhaps explaining why some of these planets have lower densities than expected by standard evolutionary models at their estimated ages.

In a previous paper (Goodman 2009, hereafter Paper I), one of us has argued that these thermally driven winds can be understood as natural heat engines, which convert a fraction of the thermal power into mechanical work: namely, the work expended to accelerate the wind. As with any other heat engine, the continual production of work must be balanced by mechanical dissipation, else the kinetic energy in the winds would grow without bound. Paper I offered a brief discussion of possible dissipation mechanisms. Here we explore those mechanisms in greater detail. The goal is to lay the foundation for subgrid models of the dissipative process suitable for use by global circulation codes.

The outline of this paper is as follows. §2 gives an overview of the dissipation mechanisms we consider. §3 presents a linear analysis of hydrodynamic Kelvin-Helmholtz instabilities of thermally stratified shear flows. We show that such flows can be destabilized by thermal diffusivity even at Richardson numbers greater than the well-known critical value $Ri_{\text{crit}} = 1/4$. Under conditions relevant to exoplanet winds, however, we estimate that the associated growth rates are too slow and the longitudinal wavelengths too long to be important for dissipation, unless $Ri < 1/4$, which requires transsonic flow unless the vertical width of the shear layer is small compared to a pressure scale height. Hence shocks may be as important as shear-driven turbulence for dissipation. To investigate this, as described in §4, we have used the ZEUS code in two dimensions to simulate a part of the atmosphere with horizontal and vertical dimensions comparable to the pressure scale height. Thermal diffusion and viscosity have been added to the code, and thermal driving of the wind is simulated by a horizontal body force with nonzero curl. We study the velocity and dissipation rate of the wind in a statistical steady state as a function of the strength of the driving compared to the acceleration of gravity. §5 discusses our results in the context of previous work on winds in jovian planets both within and beyond the solar system. §6 summarizes our main conclusions.

2. Overview of dissipation mechanisms

We begin by reviewing the physical conditions in those parts of the atmosphere where strong winds may occur. Because of the strong stellar irradiation, the temperature should be approximately constant with depth,

$$T \approx 1300 \left(\frac{fL_*}{L_\odot} \right)^{1/4} \left(\frac{a}{10R_\odot} \right)^{-1/2} \text{ K} \quad (1)$$

where L_* is the stellar luminosity, a the orbital semi-major axis, and f a dimensionless factor of order unity that depends upon the local zenith angle of the star, the albedo, and the efficiency of lateral heat redistribution ($f = 1$ for complete redistribution and negligible albedo). For a solar-mass primary, the orbital period is $P_{\text{orb}} = 3.66(a/10R_\odot)^{3/2}$ d. The sound speed in an atmosphere dominated by molecular hydrogen is $c_s \approx 2.75(T/1300 \text{ K})^{1/2} \text{ km s}^{-1}$. A characteristic circulation timescale is

$$t_{\text{circ}} = \frac{2\pi R_p}{c_s} \approx 1.85 \left(\frac{T}{1300 \text{ K}} \right)^{-1/2} \left(\frac{R_p}{R_J} \right) \text{ d}, \quad (2)$$

where R_p is the planetary radius. Assuming that the planet rotates synchronously, by this definition t_{circ} is comparable to the rotation period, as it is on Earth. Coriolis effects are likely to be important but not as dominant as on a more rapidly rotating and colder planet such as Jupiter itself.

Several considerations point to transsonic wind speeds, as discussed in Paper I. First, absent dissipation, flow along isobars from the day to the night side, starting from rest, would accelerate to

$$U \sim \sqrt{g\Delta z} \ln \frac{T_{\text{day}}}{T_{\text{night}}},$$

where $\Delta z \sim H_p = c_s^2/\gamma g$ is the range of depths over which the thermal forcing changes sign [see eq. (16)]. Indeed, repeated cycling between day and night could accelerate the wind indefinitely, were there no mechanical dissipation. Second, the strong entropy stratification tends to stabilize the flow against turbulent dissipation at small Mach numbers. And third, many numerical models of exoplanetary circulation do predict supersonic winds (see Paper I for references).

Another direct consequence of the radiatively induced temperature (1) is that the vertical density profile is approximately exponential, with a scale height $H_p = k_B T / gm_{H_2}$ that is small compared to the planetary radius:

$$\frac{H_p}{R_p} \approx 2.9 \times 10^{-3} \left(\frac{T}{1300 \text{ K}} \right) \left(\frac{R_p}{R_J} \right)^{-1} \left(\frac{g}{g_J} \right)^{-1}, \quad (3)$$

where $g = GM_p/R_p^2$ is the surface gravity and $g_J \equiv GM_J/R_{J,\text{eq}}^2 \approx 2500 \text{ cm s}^{-2}$.

The pressure at the infrared photosphere is

$$p_{\text{ph}} = \frac{2g_p}{3\kappa_{\text{R}}} \approx 1.7 \left(\frac{\kappa_{\text{R}}}{\text{cm}^2 \text{ g}^{-1}} \right)^{-1} \left(\frac{g}{g_J} \right) \text{ mbar}, \quad (4)$$

where κ_{R} is the Rosseland mean opacity appropriate to the temperature (1). A larger characteristic pressure is that at which the thermal time is comparable to t_{circ} . Taking $t_{\text{th}} = H_p^2/\chi$, where $\chi = 16\sigma T^3/\kappa\rho^2 c_P$ is the thermal diffusivity and $c_P \approx 3.5k_{\text{B}}/m_{\text{H}_2}$ the specific heat capacity, we estimate the latter pressure at

$$p_{\text{th}} \approx 70 \left(\frac{\kappa_{\text{R}}}{\text{cm}^2 \text{ g}^{-1}} \right)^{-1/2} \left(\frac{T}{1300 \text{ K}} \right)^{5/4} \left(\frac{g}{g_J} \right) \left(\frac{R_p}{R_J} \right)^{1/2} \text{ mbar}. \quad (5)$$

The Reynolds number of these winds is enormous. The dynamic viscosity of molecular hydrogen is (Stiel & Thodos 1963) $\rho\nu = 1.9 \times 10^{-4}(T/1000 \text{ K})^{0.65} \text{ g cm}^{-1} \text{ s}^{-1}$, and therefore

$$Re \equiv \frac{c_s H_p}{\nu} \approx 5 \times 10^8 \left(\frac{p}{\text{mbar}} \right) \left(\frac{T}{1300 \text{ K}} \right)^{-0.15} \left(\frac{g}{g_J} \right)^{-1}. \quad (6)$$

At pressures above a microbar at most, therefore, it is appropriate to regard the winds as inviscid.

By other dimensionless measures, however, these flows are less ideal. At these temperatures and pressures, thermal ionization of alkali metals yields magnetic Reynolds numbers $Rm \equiv c_s H_p/\eta \sim O(1)$, where η is the magnetic diffusivity. Batygin & Stevenson (2010) and Perna et al. (2010) have suggested that non-ideal MHD effects could exert a significant drag on the winds and perhaps even contribute to heating the convective interior in the presence of a background planetary magnetic field $\gtrsim 10 \text{ G}$.

A dimensionless inverse measure of thermal (rather than magnetic) diffusion is the Peclet number

$$Pe \equiv \frac{c_s H_p}{\chi} \approx 0.2 \left(\frac{p}{\text{mbar}} \right)^2 \left(\frac{\kappa_{\text{R}}}{\text{cm}^2 \text{ g}^{-1}} \right) \left(\frac{T}{1300 \text{ K}} \right)^{-7/2} \left(\frac{g}{g_J} \right)^{-1}. \quad (7)$$

Thus, at the pressure (5) where thermal and advection timescales may be comparable, $Pe \sim 10^3$, with no direct dependence on κ_{R} .

Another important dimensionless quantity is the Richardson number, which characterizes the relative strength of stratification and shear. The local Richardson number at altitude z is $Ri(z) \equiv N^2/(dU/dz)^2$, where $N(z)$ is the Brunt-Väisälä frequency [eq. (11)]. In the limit of infinite Re and Pe , a necessary condition for incompressible shear-driven instability is that

$Ri < 1/4$ somewhere in the flow (Drazin & Reid 1981). For a flow that changes smoothly by ΔU over a vertical distance Δz , a characteristic value for Ri in a constant-temperature background is, using eq. (11) and noting $H_p = c_s^2/\gamma g$,

$$Ri \approx \frac{(\gamma - 1)}{M^2 \gamma^2} \left(\frac{\Delta z}{H_p} \right)^2, \quad (8)$$

where $M = 2\Delta U/c_s$ is the Mach number associated with the amplitude of the shear profile. Thus since $\gamma \approx 7/5$ for an atmosphere dominated by molecular hydrogen, $M \gtrsim 0.9(\Delta z/H_p)$ is required for instability. This linear stability criterion can be related to an energy principle and therefore should govern nonlinear instabilities also. However, when the stratification is primarily thermal rather than compositional, as we expect for the wind zone of these atmospheres, its stabilizing influence can be undercut by diffusion of heat. Thus instability may be possible at $Ri > 1/4$ if the Peclet number (7) is not too large. One of the goals of the present study is to quantify this statement for hot-Jupiter winds.

From this survey of characteristic physical conditions and dimensionless numbers, three possible sources of mechanical dissipation for the winds come to the fore: (1) MHD effects, probably requiring $B \gtrsim 10$ G; (2) shear-driven turbulence, requiring $Ri < 1/4$ and/or moderate Pe ; and (3) shocks, requiring $M > 1$ as we have defined it. Another possibility, raised in Paper I, is the double-diffusive Goldreich-Schubert-Fricke instability (Goldreich & Schubert 1967; Fricke 1968), which we do not consider here for two reasons: first, although the linear GSF instability is axisymmetric, we believe that its saturation can be studied reliably only with high-resolution 3D simulations, whereas we limit ourselves to 2D; and second, because the instability shuts off when (in the usual cylindrical coordinates) $\partial v_\phi/\partial z = 0$ and $\partial(\varpi v_\phi)^2/\partial \varpi \geq 0$, which conditions are not inconsistent with strong vertical shears at equatorial latitudes. Nonlinear MHD effects present even greater numerical challenges. Therefore, we concentrate on Richardson turbulence and shocks.

3. Linear Analysis

We are interested in the hydrodynamic stability of a horizontal shear flow. We first consider the Boussinesq limit in which we neglect density variations except where coupled to gravity. The equations of hydrodynamics become

$$\frac{d\mathbf{v}}{dt} = -\nabla\tilde{p} + \theta\hat{\mathbf{e}}_z + \nu\nabla^2\mathbf{v}, \quad (9a)$$

$$\frac{d\theta}{dt} = -N^2\hat{\mathbf{e}}_z \cdot \mathbf{v} + \chi\nabla^2\theta, \quad (9b)$$

$$\nabla \cdot \mathbf{v} = 0. \quad (9c)$$

Here kinematic viscosity ν is taken to be a constant,

$$\theta \equiv -g \left(\frac{\partial \ln \rho}{\partial \ln T} \right)_p \frac{\delta T}{T} \rightarrow g \frac{\delta T}{T} \quad (\text{ideal gas}) \quad (10)$$

is proportional to the fractional temperature variation,

$$N^2 \equiv \frac{\rho g^2}{p} \left[\left(\frac{\partial \ln T}{\partial \ln P} \right)_s - \frac{d \ln T / dz}{d \ln P / dz} \right]_0 \rightarrow \frac{\gamma - 1}{\gamma} \frac{g}{H_p} \quad (\text{ideal gas \& } T_0 = \text{constant}) \quad (11)$$

is the square of the Brunt-Väisälä frequency of the background hydrostatic state, and the pressure scale height

$$H_p \equiv \left| \frac{d \ln p}{dz} \right|_0^{-1} \rightarrow \frac{k_B T_0}{\mu m_p g} = \frac{c_s^2}{\gamma g}. \quad (12)$$

We assume the optically thick diffusion limit for radiative transfer in which $\chi = 16\sigma T^3 / 3\kappa c_p \rho^2$. We further pick the opacity $\kappa \propto T^3 \rho^{-2}$ so that $\chi = \text{constant}$. Note that in our energy equation we assume no background temperature gradient. Other authors have studied the linear stability of the Boussinesq equations (see e.g., Gage 1973; Dudis 1974; Maslowe & Thompson 1971; Koppel 1964; Miller & Gage 1972; Gage 1972), but they do not consider in detail the destabilizing effects of thermal diffusivity in the viscous, optically thick limit. We are interested in the growth rates in the weak viscosity regime and their relevance to our numerical simulations.

Assuming a plane-parallel background state with horizontal flow

$$\theta_0 = 0 = \tilde{p}_0, \quad \mathbf{v}_0 = U(z) \hat{\mathbf{e}}_x, \quad (13)$$

we can expand all perturbations with the dependence $\exp(-i\omega t + ik_x x + ik_y y)$ to obtain the linearized 6th order system of equations

$$v_{1z}'''' = \left(\frac{ik^2 \sigma}{\nu} - k^4 - \frac{ik_x U''}{\nu} \right) v_{1z} + \left(2k^2 - \frac{i\sigma}{\nu} \right) v_{1z}'' + \frac{(k^2)}{\nu} \theta_1, \quad (14a)$$

$$\theta_1'' = \left(-\frac{i\sigma}{\chi} + k^2 \right) \theta_1 + \frac{N^2}{\chi} v_{1z}, \quad (14b)$$

where $\sigma = \omega - k_x U$, $k \equiv (k_x^2 + k_y^2)^{1/2}$, and primes denote d/dz .

We use a relaxation method to solve this system of equations, and we test our results against limiting cases of background velocity profile U and parameters ν, χ , and N^2 for which there are simple analytic solutions. See the Appendix for the limits and analytical solutions. We can nondimensionalize our parameters by defining the Richardson number as $Ri = N^2 H_p^2 / U_{max}^2$, Reynolds number $Re = H_p U / \nu$, Peclet number $Pe = H_p U / \chi$, and

Prandtl number $Pr = \nu/\chi = Pe/Re$. (In §2, we scaled Re and Pe by the sound speed rather than the flow velocity in the expectation of a Mach number of order unity, but that is not appropriate in the present Boussinesq context.) We give all our linear results in terms of these dimensionless numbers.

For the problem of interest we specify boundary conditions for the system (14) as follows. We impose $v_{1z} = 0$ at $z = \pm z_{max}$ so that the fluid perturbations do not penetrate the boundary. We further impose $v''_{1z} = -ik_x v'_{1x} - ik_y v'_{1y} = 0$, corresponding to vanishing viscous stress, and $\theta_1 = 0$, corresponding to fixed temperature, at both boundaries.

Consider now the limit $\nu \rightarrow 0, \chi \rightarrow 0$ of eqns (14)

$$v''_{1z} = \left(-\frac{k_x U''}{\sigma} + k^2 - \frac{(k^2) N^2}{\sigma^2} \right) v_{1z}. \quad (15)$$

From WKB arguments, the time taken for a wavelike disturbance to reach $z = 0$ from $z = z_1 \neq 0$ is infinite if $Ri > 1/4$. Further, from energy arguments the potential energy barrier separating two fluid elements at different heights exceeds the available kinetic energy that can be liberated if $Ri > 1/4$ (Chandrasekhar 1961). From these considerations, we expect the stratified shear flow to be stable for $Ri \gtrsim 1/4$ in the inviscid case with no thermal diffusion. As we turn up the thermal diffusivity the potential energy barrier between fluid elements at different heights can be more easily overcome, and we expect instabilities to survive to higher Richardson number. We expect there to be a critical Richardson number, above which the stratified flow is stable and below which there exist unstable Kelvin-Helmholtz like modes. We refer to this critical solution as the marginally stable mode.

For our stability analysis we pick background velocity profile $U = U_0 \tanh(z/H_p)$. Squire's theorem tells us that in the limit of vanishing thermal diffusivity the largest growth rates are obtained for $k_y H_p = 0$ (Drazin & Reid 1981), so we might expect this result to generalize to the case with thermal diffusion. In Fig 1 we show the marginally stable Richardson number as a function of $k_x H_p$ for $k_y H_p = 0, .1, .2$ and $Pe = 10, Re = 10^3$. As $|k_y H_p|$ increases, the critical Richardson number decreases for all $k_x H_p$. Growth rates at fixed Richardson number correspondingly decrease. We set $k_y H_p = 0$ hereafter because we are interested in the fastest growing modes. Note that we find two distinct instabilities at long and short wavelengths. The long wavelength instabilities have *not* converged with z_{max} . The solid lines indicate solutions computed with $z_{max} = 3H_p$, and the dashed line indicates a solution computed at $z_{max} = 5H_p$. The long wavelength instability is driven to longer wavelengths as z_{max} increases. We run into similar issues encountered by Dudis (1973) in the long wavelength limit. We must integrate to larger and larger z_{max} or use an appropriate asymptotic boundary condition as $k_x H_p \rightarrow 0$ to obtain better convergence.

Although our code has not converged for long wavelengths, our results suggest that there

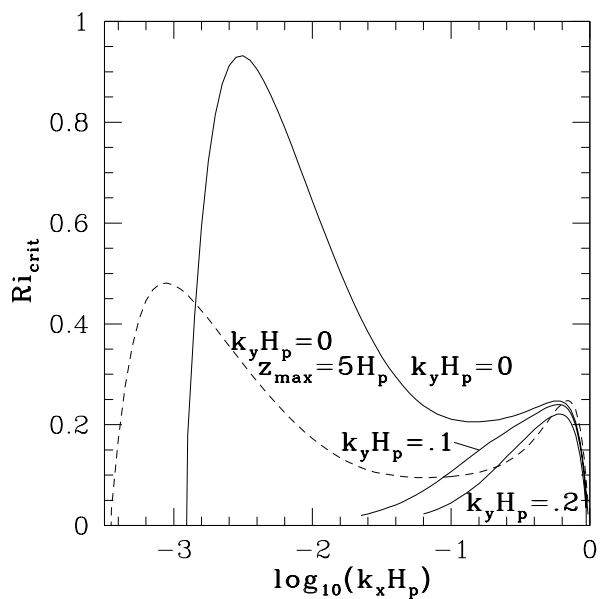


Fig. 1.— Marginally stable Richardson number as a function of $k_x H_p$ for $Pe = 10$, $Re = 10^3$, and at a sequence of $|k_y H_p| = 0, .1, .2$. As $|k_y H_p|$ increases the critical Richardson number decreases at all $k_x H_p$. The dashed curve shows a separate run at $z_{\text{max}} = 5H_p$, indicating the long wavelength results have not converged.

may be a real inviscid instability in the limit $k_x H_p \rightarrow 0$. This is demonstrated analytically in Appendix B. The dimensionless form of the equations of motion given in the Appendix suggest that the long-wavelength modes should be sensitive to the combination of parameters $Pe Ri k z_{\max}^2 / H_p$, and the analysis guarantees the existence of the long-wavelength modes only where this combination is $\ll 1$; some version of the long-wavelength modes may exist more generally, but we have not proven it. So it is not surprising that our numerical results for these modes have not converged with respect to z_{\max} .

In Fig 2 we show the critical Richardson number as a function of $k_x H_p$ at $Re = 10^3$ and at a sequence of Peclet numbers. As the Peclet number decreases below ~ 40 , the long wavelength instability begins to strengthen and survive above $Ri = 1/4$. The dashed line is a run at higher $z_{\max} = 5H_p$ and shows the convergence of short wavelength results. As the Peclet number decreases below ~ 2.5 the flow at short wavelengths begins to destabilize above $Ri = 1/4$. For high Reynolds number and high Peclet number our short wavelength results are in rough agreement with the inviscid results of Dudis (1974). There are quantitative differences due to our assumption of an isothermal background temperature profile.

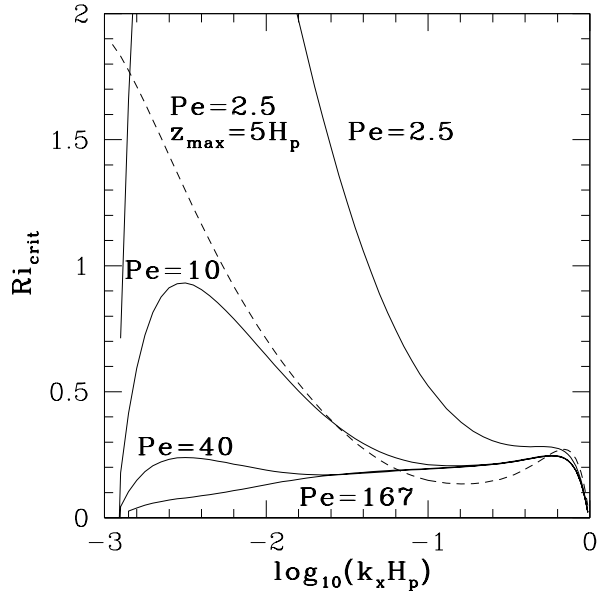


Fig. 2.— Marginally stable Richardson number vs. wavenumber $k_x H_p$, for fixed Reynolds number $Re = 10^3$ and a sequence of Peclet numbers $Pe \equiv (\nu/\chi)Re$. At $Pe \lesssim 40$, a long-wavelength instability that survives at $Ri > 1/4$ develops. At $Pe \lesssim 2.5$, the short-wavelength modes destabilize above $Ri = 1/4$. The dashed curve indicates a run at higher $z_{\max} = 5H_p$. The short-wavelength results have converged reasonably well, and for $Pe \sim 10^2 - 10^4$, the critical Richardson number remains fixed at $Ri = 1/4$.

In Fig 3 we show the growth rates of the modes with $Ri = \frac{1}{2} Ri_{\text{crit}}$ as a function of $k_x H_p$, for fixed $Re = 10^3$ and at a sequence of Peclet numbers. The long wavelength growth rates at $k_x H_p = 3.2/Re$ are well over two orders of magnitude smaller than shorter wavelength growth rates. This result agrees with our estimation that the inviscid instability in the limit $k_x H_p \rightarrow 0$ has weak growth rate. For our numerical simulations we will be primarily interested in the more unstable short wavelength instabilities that have maximum growth at $k_x H_p \sim 0.5$. Note that Ri_{crit} increases with decreasing Pe , so we are computing growth rates at higher Richardson number for the lower Peclet number curves. At fixed Ri , growth rates increase with decreasing Pe , as we expect from simple heat diffusion arguments.

We conclude from Figs 2 and 3 that the linear growth rates of the fastest growing mode are unchanged in the parameter regime we are interested in, $Pe \sim 10^2 - 10^4$.

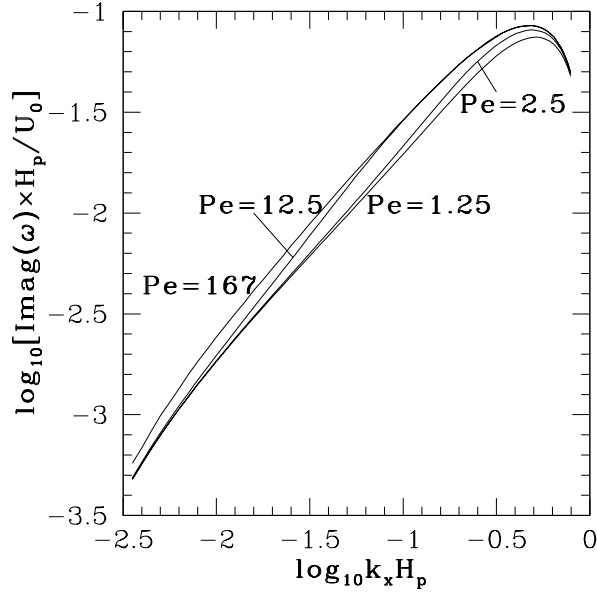


Fig. 3.— Growth rates of modes with $Ri = \frac{1}{2} Ri_{\text{crit}}$ as a function of $k_x H_p$, for fixed $Re = 10^3$ and $Pe = 1.25, 2.5, 12.5, 167$. The long wavelength instability that survives to high Richardson number has growth rates over two orders of magnitude weaker than shorter wavelength growth rates.

4. Numerical Simulations

We use ZEUS-2D v2.0 (Stone & Norman 1992) to run hydrodynamical simulations of a horizontal wind profile in a local equatorial section of the atmosphere. Cartesian coordinates x and z correspond to longitude and altitude, respectively, each extending over a few pressure scale heights: typically $20H_p \times 5H_p$. Longitude x is periodic, though with a period much less than the true circumference of the planet. The simulations include vertical gravity, thermal diffusion of heat, shear viscosity, and a horizontal body force per unit volume $\rho f(z)\hat{\mathbf{e}}_x$ [eqs. (17) & (19)] rather than thermal forcing. A few words of justification are in order.

The pressure acceleration is nonpotential due to longitudinal entropy gradients; the component of its curl normal to the equatorial plane is, in spherical coordinates $r\theta\phi$,

$$\hat{\mathbf{e}}_\theta \cdot (\nabla \rho^{-1} \times \nabla p) = \frac{1}{r\rho^2} \left(\frac{\partial \rho}{\partial T} \right)_p \left[\frac{\partial T}{\partial \phi} \frac{\partial p}{\partial r} - \frac{\partial p}{\partial \phi} \frac{\partial T}{\partial r} \right] \approx \frac{g}{r} \left(\frac{\partial \ln T}{\partial \phi} \right)_p, \quad (16)$$

in which the final form uses the ideal-gas law and assumes approximate vertical hydrostatic equilibrium. This curl must vanish in the (nearly isentropic) convection zone. Furthermore, since thermal forcing by itself does not add any net momentum to the flow,¹ the nonpotential longitudinal force must reverse sign with depth within the radiative atmosphere. In fact one expects this nonpotential “battery” to be concentrated at pressures $\lesssim p_{\text{th}}$ [(5)], which is quite shallow compared to the radiative-convective interface, typically \sim kbar. The nonpotential force must also reverse sign at least twice in longitude because (16) is periodic in ϕ , but the horizontal scale of variation of this force is probably small compared to its vertical scale since the radiative atmosphere is thin. Hence the profile (19), which is horizontally constant and extends over $\sim 2H_p$ vertically, reversing sign within this depth, is a plausible representation of the horizontal forcing within our local computational domain.

4.1. Setup

The source terms for momentum and energy in ZEUS are modified by the addition of the terms within square brackets below:

$$\rho \left(\frac{\partial \mathbf{v}}{\partial t} \right)_{\text{sources}} = -\nabla p - \rho g \hat{\mathbf{e}}_z - \nabla \cdot \mathbf{Q} + [\rho f(z)\hat{\mathbf{e}}_x + \nabla \cdot \boldsymbol{\sigma}'] \quad (17)$$

¹Arras & Socrates (2010) have suggested, however, that in conjunction with the tidal field of the host star, thermal forcing may lead to net torques on the planet.

and

$$\left(\frac{\partial e}{\partial t}\right)_{\text{sources}} = -p\nabla \cdot \mathbf{v} - \mathbf{Q} \cdot \nabla \mathbf{v} + [\nabla \cdot (\chi \rho c_p \nabla T) + \boldsymbol{\sigma}' \cdot \nabla \mathbf{v}], \quad (18)$$

in which $\boldsymbol{\sigma}'$ is the viscous shear tensor, with components

$$\sigma'_{ik} = \nu \rho \left(\frac{\partial v_i}{\partial x_k} + \frac{\partial v_k}{\partial x_i} - \frac{2}{3} \delta_{ik} \frac{\partial v_l}{\partial x_l} \right),$$

where ν and g are taken to be constants. ZEUS' standard von Neumann & Richtmyer artificial viscosity tensor \mathbf{Q} is applied with shocks spread over ≈ 2 zones. The thermal diffusivity χ is again given in the optically thick limit by $\chi = 16\sigma T^3/3\kappa c_p \rho^2 = \text{const}$; constant χ would correspond therefore to $\kappa \propto T^3 \rho^{-2}$. The horizontal forcing profile is

$$f(z) = \epsilon g \left[2\text{sech}^2(z/H_p) \tanh(z/H_p) + \alpha \text{sech}^2(z/H_p) \right], \quad (19)$$

where H_p is the pressure scale height, α is a parameter that we adjust to ensure zero net momentum input on our grid, and $\epsilon \ll 1$ determines the overall strength of the forcing. This form is motivated by the viscous acceleration on a fluid with hydrostatic density profile and horizontal velocity profile given by $v_x = U_0 \tanh(z/H_p)$. The viscous acceleration in this case is given by $\epsilon g = \nu U_0/H_p^2$ and $\alpha = 1$. We use an FTCS differencing scheme for our modified source terms, and the ZEUS timestep constraint must satisfy $\delta t < \delta t_\nu = (\Delta x)^2/4\nu$ and $\delta t < \delta t_\chi = (\Delta x)^2/4\chi$ for stability. We are interested in $Pr < 1$, so the latter constraint is a tighter restriction on δt . But $\delta t_\chi/\delta t_{CFL} \approx Pe/4N_p$, where N_p is the number of grid points per pressure scale height and Pe is the Peclet number in the flow. Dimensionless parameters for our numerical results are scaled to the sound speed c_s as in §2. Our simulations generally satisfy $Pe \sim 10 - 100$ and $N_p \sim O(10)$, so $\delta t_\chi/\delta t_{CFL} \sim O(1)$ and the diffusion and CFL timesteps are usually comparable.

As stated, x is periodic. At $z = z_{\min}$ and z_{\max} , we impose reflecting conditions for density and velocity and constant temperature $T = T_{\text{wall}}$. We initialize the density to $\rho(x, z) = \rho_0$ and the internal energy density to $e(x, z) = e_0$, allowing the flow to settle under the influence of gravity. The velocity is initialized to $\vec{v} = U_0 \tanh(z/H_p) \hat{\mathbf{e}}_x$. The wall temperature is set to the initial grid temperature, $T_{\text{wall}} = T_0 = (e_0/\rho_0)\mu m_p(\gamma - 1)/k_B$. We pick $\rho_0 = 1, e_0 = .01, \gamma = 1.4$, and $g = .004$. Our simulations are run over 5 vertical pressure scale heights, from $z = -2.5H_p$ to $z = 2.5H_p$. The density at the base of our simulation if it were in hydrostatic equilibrium is then $\rho_{\text{base}} = 5\rho_0$. The code units for our problem are given in table 1. We nondimensionalize parameters according to these units.

We run our simulations over 20 scale heights in the horizontal direction. We are physically interested in $Pe^{-1} \approx 10^{-2} - 10^{-4}$, $Re^{-1} \rightarrow 0$, but the viscosity must be large enough to maintain energy conservation, and $\epsilon \leq 10^{-2}$. In the absence of a shear viscosity the grid

loses energy to numerical dissipation at the grid scale. We must pick ν large enough such that the viscous dissipation length $l_\nu \sim (|\partial_j v_i|/\nu)^{-1/2}$ is larger than the grid scale, and the dissipation of solenoidal turbulence is converted to internal energy. Our standard runs have $N_p = 10$ grid points per pressure scale height, but for certain runs which conserve energy less well we use up to $N_p = 30$ grid points per pressure scale height.

4.2. Tests

We run two simple test problems to verify proper implementation of the horizontal forcing and viscosity. Using a simplified shear viscosity $\partial v/\partial t = \nu \nabla^2 v$ and no viscous heating, there is an exact solution for the viscous decay of initial velocity profile given by $U(z, 0) = \text{sign}(z)\hat{e}_x$. The velocity is given at later times by $U(z, t) = \text{erf}(z/2\sqrt{\nu t})\hat{e}_x$. Again using this simplified shear viscosity and horizontal forcing given by $f(z) = \epsilon 2\text{sech}^2(z/H_p) \tanh(z/H_p)$, there is an exact laminar solution for the velocity profile. The laminar solution satisfies $0 = f(z) + \nu U''(z)$, where $U(z) = (\epsilon H_p^2/\nu) \tanh(z/H_p)$. We conclude from these two tests that there is negligible numerical dissipation in the laminar regime. We can also use the latter to estimate the wind speed in the laminar regime when the viscous heating is implemented.

We are interested in the behavior of the solutions to eqns 17 and 18 at different forcing amplitudes. We check that the parameter α has a second order effect on the forcing and that we can roughly characterize the amplitude of the forcing by the single parameter ϵ .

4.3. Diagnostics of dissipation

We must also maintain energy conservation in our simulations. We are continually injecting energy onto the grid via the horizontal forcing, and to reach a statistical steady state this energy must first be converted into internal energy and then allowed to diffuse through the boundary walls. Because ZEUS is not based on a conservative form of the energy equation, numerical diffusion dissipates kinetic energy on the grid scale without converting it

Table 1. Code Units.

Unit	Length	Time	Density	Acceleration
Value	$H_p = 1$	$t = H_p/c_s = 13.36$	$\rho_{base} = 5$	$g = .004$

to internal energy; to avoid this, it is necessary to add an explicit shear viscosity (in addition to the artificial bulk viscosity used to mediate shocks).

We compute a fractional energy error

$$\frac{\dot{E}}{\dot{E}_{\text{in}}} = \frac{\dot{E}_{\text{in}} - \dot{E}_{\text{kin}} - \dot{E}_{\text{int}} - \dot{E}_{\text{grav}} - \dot{E}_{\text{out}}}{\dot{E}_{\text{in}}}, \quad (20)$$

where

$$\begin{aligned} \dot{E}_{\text{in}} &= \iiint \rho v_x f(z) dx dz & \dot{E}_{\text{kin}} &= \frac{d}{dt} \iiint \frac{1}{2} \rho v^2 dx dz & \dot{E}_{\text{int}} &= \frac{d}{dt} \iiint e dx dz \\ \dot{E}_{\text{out}} &= \int \left[-\rho c_p \chi \frac{\partial T}{\partial z} \right]_{z_{\text{min}}}^{z_{\text{max}}} dx & \dot{E}_{\text{grav}} &= \frac{d}{dt} \iiint \rho g z dx dz \end{aligned}$$

We briefly mention here a number of strategies that we use to improve energy conservation. The fractional energy error will tend to decrease if we keep the amplitude of the forcing function lower so that there is less energy injection onto the grid. In a similar vein, if we localize the forcing function to the shear layer as opposed to distributing it over the entire vertical extent of the grid then there will be less energy injection and better energy conservation. Other strategies include increasing the kinematic viscosity or making the grid resolution finer in order to capture kinetic energy dissipation above the grid scale via the explicit viscosity. Finally, we can increase the thermal diffusivity so as to allow excess internal energy to diffuse off the grid. These considerations must be balanced against keeping the computation time reasonably low and keeping the solutions physically relevant to the problems of interest.

We consider that a statistical steady state is reached when $\langle \dot{E}_{\text{int}} \rangle_t$, $\langle \dot{E}_{\text{kin}} \rangle_t$, and $\langle \dot{E}_{\text{grav}} \rangle_t$ are all $\ll \dot{E}_{\text{in}}$, and when the Mach number [eq. (24)] and the rms vertical velocity $\langle v_z^2 \rangle_{x,y}^{1/2}$ are constant for at least a horizontal sound crossing time, $20H_p/c_s$. In steady state, $\dot{E}/\dot{E}_{\text{in}} \approx (\dot{E}_{\text{in}} - \dot{E}_{\text{out}})/\dot{E}_{\text{in}}$. We maintain the fractional energy error to within ten percent.

Dissipation of kinetic energy involves production of entropy. If s is entropy per unit mass, then

$$\rho \frac{Ds}{Dt} = \frac{-\mathbf{Q} : \nabla \mathbf{v} + \boldsymbol{\sigma}' : \nabla \mathbf{v}}{T} + \chi_{c_p \rho} |\nabla \ln T|^2 + \nabla \cdot (\chi_{c_p \rho} \nabla \ln T).$$

When integrated over our computational domain, the final term is $-\dot{E}_{\text{out}}/T_{\text{wall}}$, \dot{E}_{out} being the rate of escape of heat. So

$$\dot{E}_{\text{out}} = T_{\text{wall}} \int [T^{-1}(-\mathbf{Q} : \nabla \mathbf{v} + \boldsymbol{\sigma}' : \nabla \mathbf{v}) + \chi_{c_p \rho} |\nabla \ln T|^2] d^2 \mathbf{x} + \frac{d}{dt} \iint \rho s dx dy. \quad (21)$$

In statistical steady state, the time average of the last term vanishes.

While conversion of mechanical energy to heat ultimately depends upon the “microscopic” processes in eq. (21), we gain insight into the macroscopic processes that remove kinetic energy from the large-scale flow—shocks and turbulence—by monitoring the energy change in each operator split source step. The price paid for this approach is having to deal with a mixture of reversible and irreversible effects. Under adiabatic conditions, for example, the compressive heating term $\dot{E}_{pdV} = \int -p \nabla \cdot \mathbf{v} d^2 \mathbf{x}$ would be completely reversible, but shocks and thermal diffusion make $\langle \dot{E}_{pdV} \rangle \neq 0$ even in steady state. There is also a change in gravitational potential energy $\dot{E}_{grav} = \int v_z \rho g d^2 \mathbf{x}$ associated with the vertical gravity source step. In many of our runs we find that \dot{E}_{pdV} and \dot{E}_{grav} have large oscillations that nearly cancel. Using integration by parts, one can show that

$$\dot{E}_{pdV} + \dot{E}_{grav} = \iiint \mathbf{v} \cdot [\rho \nabla (gz) + \nabla p] dx dz. \quad (22)$$

Thus the near cancellation suggests that our flows are close to vertical hydrostatic equilibrium despite large vertical motions. We find it easiest to monitor the combination $\dot{E}_{pdV} + \dot{E}_{grav}$. The time average of this term is largely the work done to mix the fluid vertically; absent thermal diffusion, this could lead to an almost adiabatic temperature-pressure profile, $\partial \ln T / \partial z \approx -(\gamma - 1)g/c_s^2$, but in steady state diffusion tends to restore the stratification. Thus vertical mixing acts as a refrigerator—a heat engine in reverse—absorbing mechanical work to drive heat up the temperature gradient.

Shock dissipation is dominated by the artificial bulk viscosity, $\dot{E}_{abv} = \int -\mathbf{Q} \cdot \nabla \mathbf{v} d^2 \mathbf{x}$ but receives small contributions also from the shear stress and from the \dot{E}_{pdV} term.

Since we find that shocks are weak, we can estimate the turbulent energy dissipation rate as

$$\langle \dot{E}_{\text{turb}} \rangle_t \approx \langle \dot{E}_p \nabla \cdot \mathbf{v} + \dot{E}_{\text{grav}} \rangle_t + \langle \dot{E}_\nu \rangle_t - \langle \dot{E}_{\text{lam}} \rangle_t, \quad (23)$$

where $\dot{E}_\nu = \int \boldsymbol{\sigma}' \cdot \nabla \mathbf{v}$ and $\dot{E}_{\text{lam}} = \int \nu \rho (\partial \bar{v}_x / \partial z)^2 d^2 \mathbf{x}$. Assuming an effective turbulent viscosity acting on the time-averaged mean shear profile, we estimate the turbulent dissipation rate as $\langle \dot{E}_{\text{turb}} \rangle_t = \langle \int \nu_t \rho (\partial \bar{v}_x / \partial z)^2 d^2 \mathbf{x} \rangle_t$. The effective shear viscosity due to turbulence in a flow that does not resolve the turbulent energy cascade is then $\nu_t = \nu \langle \dot{E}_{\text{turb}} \rangle_t / \langle \dot{E}_{\text{lam}} \rangle_t$.

4.4. Results

Figs 4,5, and 6 respectively give the run of Mach number, defined in eq. (24), rms vertical velocity, and fractional energy error versus $\nu/c_s H_p$ for $\chi/c_s H_p = 0.094$, $\epsilon = 0.1$. The Prandtl number is less than one for all of these runs. Note the presence of four distinct

solutions at $\nu/c_s H_p > 10^{-3}$. There is a fast solution, denoted by filled triangles, a medium velocity solution, denoted by filled squares, and two slow solutions, denoted by filled circles and open stars. Where solution branches overlap, we trace each branch by starting from a representative member and then gradually varying parameters. We use a similar parameter deformation to verify that each branch is limited to a certain range of $\nu/c_s H_p$ as indicated in Figs 4-6.

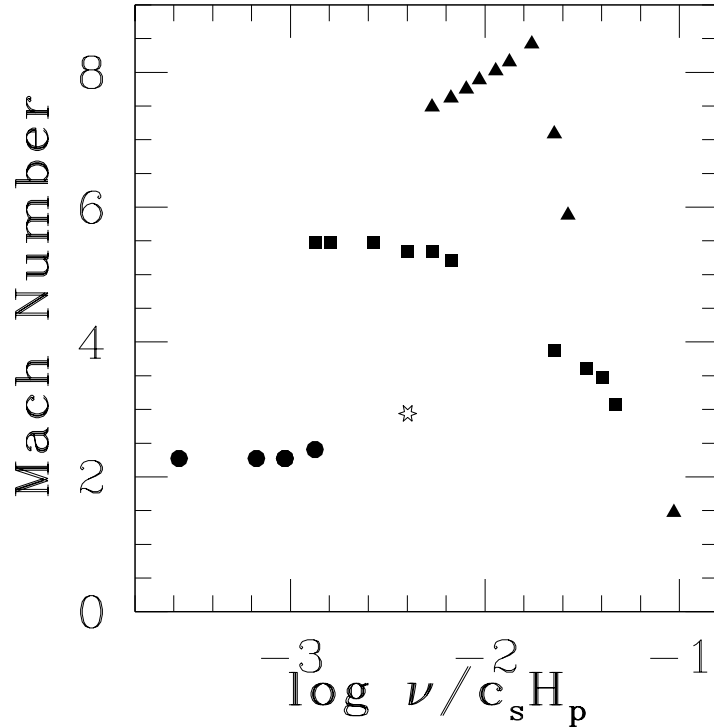


Fig. 4.— Wind amplitude as a function of scaled viscosity $\nu/c_s H_p$ for $\epsilon = 0.1, \chi/c_s H_p = 0.094$. We find four distinct solutions in the range $\log_{10} \nu/c_s H_p = -3$ to -1.5 , but a unique solution, with Mach number $\mathcal{M} \sim 2.3$, in the high- Re limit.

The solutions differ in the importance of laminar, turbulent, shock, and irreversible compressional dissipation. The fast solutions (triangles) have high laminar energy dissipation. Fig 5 indicates that there is a significant vertical component to the velocity field, but the bulk of the viscous dissipation is laminar rather than turbulent. This is reflected by wavelike oscillations in the flow as opposed to turbulent Kelvin-Helmholtz rolls. The medium and slow B solutions have stronger irreversible compressional heating and shocks, but they still have relatively high laminar dissipation. For the planetary wind problem of interest to us this laminar dissipation is unphysical, and as we increase the Reynolds number these solutions disappear. We conclude that these unphysical solutions are supported by

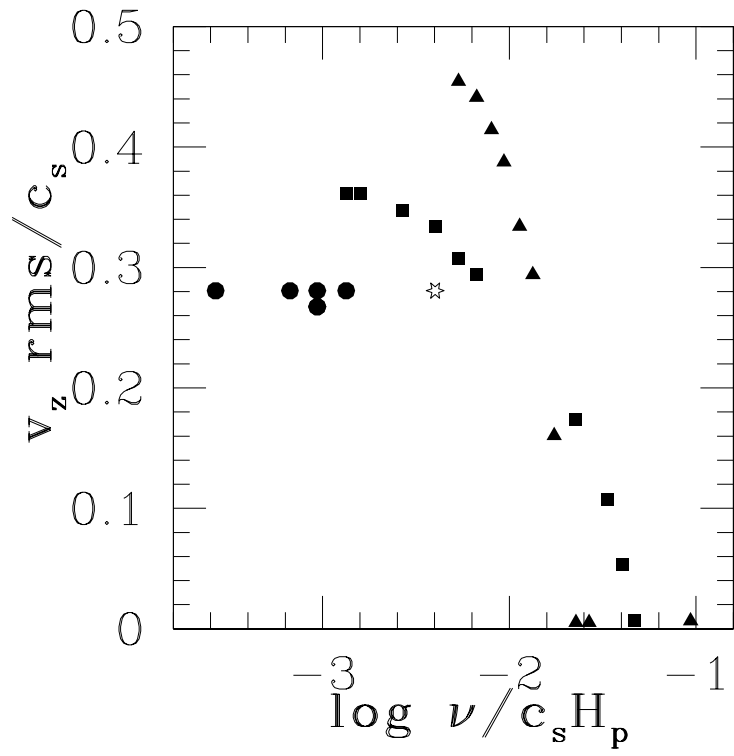


Fig. 5.— Scaled vertical velocity fluctuations as a function of $\nu/c_s H_p$ for $\epsilon = 0.1, \chi/c_s H_p = 0.094$.

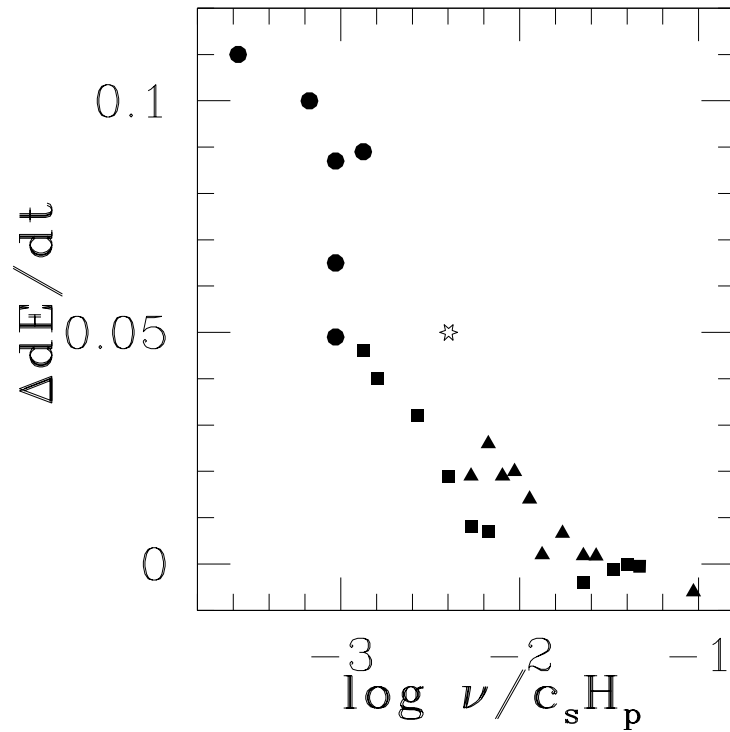


Fig. 6.— Fractional energy error as a function of $\nu/c_s H_p$ for $\epsilon = 0.1, \chi/c_s H_p = 0.094$. The extra two lower filled circles at $\log_{10} \nu/c_s H_p = -3.03$ demonstrate the convergence of our slow A solutions. The energy error decreases with increased resolution, but the gross properties of the flow remain unchanged.

the shear viscosity. Numerical diffusion can also support these unphysical solutions. At a grid resolution of $N_p = 3$ grid points per pressure scale height and parameters from Fig 4, we find unphysical solutions even at $\nu/c_s H_p = 0$. We estimate that it is necessary to have $N_p \gtrsim O(10)$ in order to enter the high- Re regime where there exists a single, physical solution. This unique solution is the slow A solution in Figs 4 - 6. It is characterized by weak laminar dissipation and strong irreversible compressional and shock dissipation. We check the convergence of this solution with runs at 1.5 and 2 times the standard resolution. Extra filled circles at $\log_{10} \nu/c_s H_p = -3.03$ in figs 4 - 6 indicate higher resolution runs. The wind speeds and rms vertical velocities overlap, but the energy errors progress downwards at higher resolution.

We summarize these results in Table 2 by providing quantitative diagnostics for each solution type. We give the shear viscosity, turbulent viscosity, relative importance of artificial bulk viscosity, relative importance of turbulent dissipation, Mach number, and Richardson number for a representative solution of each type. The laminar and turbulent energy dissipation rates are directly proportional to the quoted shear and turbulent viscosities, as described in §4.3. At this stage we are only providing rough diagnostics to characterize each solution type, but we infer that shocks contribute weakly to the irreversible compression because the artificial-bulk-viscosity dissipations are relatively small. The Mach number is computed as

$$\mathcal{M} \equiv \max_z \left[\frac{\int \rho(x, z) v_x(z) dx}{c_{s, \text{wall}} \int \rho(x, z) dx} \right] - \min_z \left[\frac{\int \rho(x, z) v_x(z) dx}{c_{s, \text{wall}} \int \rho(x, z) dx} \right]. \quad (24)$$

We compute the minimum Richardson number in our flows via

$$Ri = \min_z \frac{N^2}{(\partial \bar{U} / \partial z)^2} = \min_z \left[\frac{\bar{p}}{\bar{\rho}} \left(\frac{\partial \ln \bar{p}}{\partial z} \right)^2 \left(\frac{\partial \bar{U}}{\partial z} \right)^{-2} \left(\nabla_{\text{ad}} - \frac{d \ln \bar{T}}{d \ln \bar{p}} \right) \right],$$

where overbar denotes horizontal average. The fastest and medium solutions are convective near the top wall. This is due to the higher wind speed and energy injection, which cause a steeper temperature gradient there.

Fig. 4 shows that the fastest triangle solution in the laminar regime has wind speed scaling roughly as $1/\nu$, as we expect from our tests in §4.2. Further, the perfectly laminar solution at $\nu/c_s H_p = -1.03$ has $Ri = 0.36$, and we check that it should be linearly stable as well. From our runs at lower forcing we determine that for the fastest (triangle) solution, the viscosity that maximizes the wind speed scales in proportion to the forcing: $\nu_{\text{peak}}/c_s H_p \propto \epsilon$. The peak wind itself decreases only marginally. We can understand this behavior by assuming a steady-state balance between laminar dissipation of the mean flow and the forcing (19). These solutions are able to reach such a high wind speed because they are nearly laminar, until turbulent dissipation kicks in at low ν .

We map the solution space at lower forcing and thermal diffusivity and verify that there are four different solutions in the regime $Pr \lesssim 1$. Specifically, we looked at $\chi/c_s H_p = 0.094$ and $\epsilon = .025, .05$, and 0.1 , and also at $\chi/c_s H_p = 0.047, \epsilon = 0.1$. These parameters correspond to the four values in the first three rows of table 3, discussed in greater detail below. There are small quantitative differences in the results at $\chi/c_s H_p = 0.047, \epsilon = 0.1$. The fastest solution in particular has peak horizontally averaged Mach number $\sim 15\%$ higher. From our linear analysis we expect little difference in the results for any Peclet number in the range $Pe > 10$. In our simulations we are continually injecting energy onto our grid though, and the diffusivity affects how this energy is redistributed. We attribute the differences in the nonlinear behavior for $Pe \sim O(10)$ to the important dynamical effect of this internal energy redistribution.

The main takeaway point from these runs at different forcing and thermal diffusivity is that in the high-Reynolds-number limit there is a unique solution, for which the direct viscous dissipation of the mean flow is negligible compared to turbulent and shock dissipation. Further, if the grid resolution is insufficiently low, with $N_p \lesssim O(3)$, we may lock onto an artificially fast solution, even at $\nu/c_s H_p = 0$. We check the latter result for the range of parameters we studied and not just for those relevant to Fig. 4.

We now attempt to extract an effective turbulent viscosity from the physically relevant slow A solution. First note that the energy errors in Fig 6 are largest for the slow A solutions. In order to decrease the numerical dissipation we can either increase the shear viscosity $\nu/c_s H_p$ or we can make the grid resolution finer. We cannot increase the shear viscosity indefinitely because we will enter the multiple-solution regime (Fig. 4) or the laminar viscosity will become large enough to modify the properties of the solution. We must balance this against the increased computational cost of running the simulations at higher resolution. To

Table 2. Viscosity, turbulent viscosity, relative importance of artificial bulk viscosity, relative importance of turbulent dissipation, Mach number, and Richardson number for a characteristic solution of each type in Fig 4.

Solution type	$\log_{10}\nu/c_s H_p$	$\nu_t/c_s H_p$	$\langle \dot{E}_{\text{abv}} \rangle_t / \langle \dot{E}_{\text{in}} \rangle_t$	$\langle \dot{E}_{\text{turb}} \rangle_t / \langle \dot{E}_{\text{in}} \rangle_t$	\mathcal{M}	Ri
Fastest (triangle)	-2.17	0.006	0.07	0.43	7.6	< 0
Medium (square)	-2.57	0.010	0.22	0.60	5.5	< 0
Slow A (circle)	-3.03	0.015	0.13	0.79	2.3	0.033
Slow B (star)	-2.40	0.017	0.12	0.67	2.9	0.024

calculate the turbulent viscosity we use sufficiently high grid resolution and shear viscosity such that the numerical energy dissipation rate is $\lesssim 5\%$ of the energy injection rate, but shear viscosity is low enough such that the gross properties of the solution are not modified.

In Tables 3 and 4 we give the Mach number and turbulent viscosity for a series of slow A solutions at different horizontal forcing amplitudes and thermal diffusivities. The exact value of the explicit viscosity we use is unimportant, so long as the viscous dissipation length is larger than the grid scale and the viscosity is small enough to leave the gross properties of the slow A solution unmodified. In general the runs satisfy $Re > 10^3$. The runs at $\chi/c_s H_p = 0.094$ and $\epsilon = 0.025, 0.01$ are done at the standard resolution of $N_p = 10$ grid points per pressure scale height. The rest are done at twice the standard resolution (i.e., twice as many points in each dimension), with the exception of the run at $\chi/c_s H_p = 0.013$, $\epsilon = 0.01$, which is done at three times the standard resolution, and the run at $\chi/c_s H_p = 0.094$, $\epsilon = 0.005$, which is done at 1.5 times the standard resolution. We emphasize that these values of N_p indicate the grid resolution required at each set of parameter values to conserve energy within 5%, not the resolution required to find the slow A solution at $\nu/c_s H_p = 0$. At the standard resolution of $N_p = 10$, we still find the slow A solution at $\nu/c_s H_p = 0$ for all parameters surveyed, but the fractional energy error may be as large as 0.3 for the lowest diffusivity runs.

The Mach number decreases gradually with forcing amplitude ϵ for $\epsilon = 0.1$ down to $\epsilon = 0.01$, and is roughly independent of ϵ for $\epsilon = 0.005 - 0.01$. It is also independent of the diffusivity strength for $Pe \sim 10 - 100$, at all forcing amplitudes surveyed. The latter is consistent with our linear analysis, and we attribute this result to the lower energy injection rate as compared to the faster solutions from Fig. 4. There is less thermal redistribution of heat in the slow A solutions.

Fig. 7 shows the Mach number as a function of time for the run at $\epsilon = 0.01$ and $\chi/c_s H_p = 0.013$. The run has reached a statistical steady state after time $\sim 10H_p/c_s$. The steady state is characterized by a drive-up phase in which the Mach number gradually rises, and a short slowdown phase in which the Mach number rapidly drops. In Fig. 8 we show the relative contributions of dissipation due to artificial bulk viscosity and turbulence, as defined in §4.3. Both dissipation terms are confined to the slowdown phases. Shocks appear briefly during slowdown, but the majority of the kinetic energy dissipation occurs in the absence of shocks. We thus conclude that shocks do not significantly contribute to the irreversible compressional heating.

We now characterize the nature of the sharp slowdown phases that limit the wind speed in our flow. The drive-up phase is relatively smooth with small changes in the state variables across the flow. Fig. 9 shows the velocity vector field with temperature contours from T_{wall}

Table 3. Mach number for a sequence of slow A solutions at different diffusivity and horizontal forcing.

ϵ	$\chi/c_s H_p$		
	.094	.047	.013
.1	2.3	2.3	
.05	1.9		
.025	1.7		
.01	1.7	1.6	1.7
.005	1.5	1.7	1.7

Table 4. Turbulent viscosity $\nu_t/c_s H_p$ for a sequence of slow A solutions at different diffusivity and horizontal forcing.

ϵ	$\chi/c_s H_p$		
	.094	.047	.013
.1	0.015	0.017	
.05	0.010		
.025	0.0061		
.01	0.0024	0.0023	0.0024
.005	0.0012	0.0011	0.0010

to $T_{\max} = 1.07T_{\max}$ for the starred point from Fig. 7. At a short time before reaching the peak wind speed, $t \approx 0.2H_p/c_s$, a vigorous instability with 3 wavelengths in our box develops. Fig. 10 shows the velocity vector field with temperature contours from T_{wall} to $T_{\max} = 1.46T_{\max}$ for the boxed point from Fig. 7. The unstable mode is clearly visible in the temperature profile roughly halfway through the slowdown phase. Note the shocks at $z/H_p < -1$ and $x/H_p = -4.5, 2, 8.5$. Following our previous determination that the shocks are weak, we conclude that turbulent mixing associated with this unstable mode is the primary agent for dissipating kinetic energy and reducing the wind speed.

The dimensions of our box enforce a periodicity under the transformation $x \rightarrow x + 20H_p$. If the unstable mode is an ordinary Kelvin-Helmholtz mode, then from our linear analysis the only modes that can grow have either 1, 2, or 3 wavelengths in the box. Apparently the mode with 3 wavelengths and wavenumber $k_x H_p \approx .94$ is the fastest growing of the three. The Richardson numbers satisfy $Ri < 1/4$. We verify that the growth of this instability and its effect on the wind speed are independent of the dimensions of our domain. We increase the horizontal extent of our box from $L_x = 20H_p$ to $L_x = 30H_p$ and $L_x = 40H_p$ and verify the presence of this instability. At $L_x = 30H_p$ the fastest growing modes have 3 or 4 wavelengths in the box, and at $L_x = 40H_p$ they have 4 or 5 wavelengths. These wave numbers are roughly consistent with our linear analysis. More importantly though, the time-averaged Mach number of the flow remains unchanged.

5. Discussion

Ultimately we would like to provide a dissipation prescription for global simulations that do not resolve the turbulent nature of the wind profile. We first note that from Fig 7 we find a horizontally and time averaged Mach number $\mathcal{M} \sim 1.7$ and peak horizontally averaged Mach number $\mathcal{M} \sim 2.7$. The peak occurs just before the rapid growth of instabilities, and so the latter corresponds to the absolute peak Mach number in the flow. Global simulations are often more strongly supersonic. For example, the model of HD 209458b by Cooper & Showman (2005) finds $v_{\max} \approx 9 \text{ km s}^{-1}$ at the 2.5 mbar level (see Paper I for a survey of the calculations prior to 2009).

Most of these studies of global circulation employ reduced equations of motion based on the approximation of vertical hydrostatic equilibrium: shallow-water, equivalent barotropic, or primitive equations. This is done in order to cope efficiently with the large ratio of horizontal to vertical scales [eq. (3)], but the approximations used also have the effect of filtering out sound waves and shocks (even horizontally propagating ones). Such codes cannot directly represent the shocks and turbulent vertical motions studied here, although they can

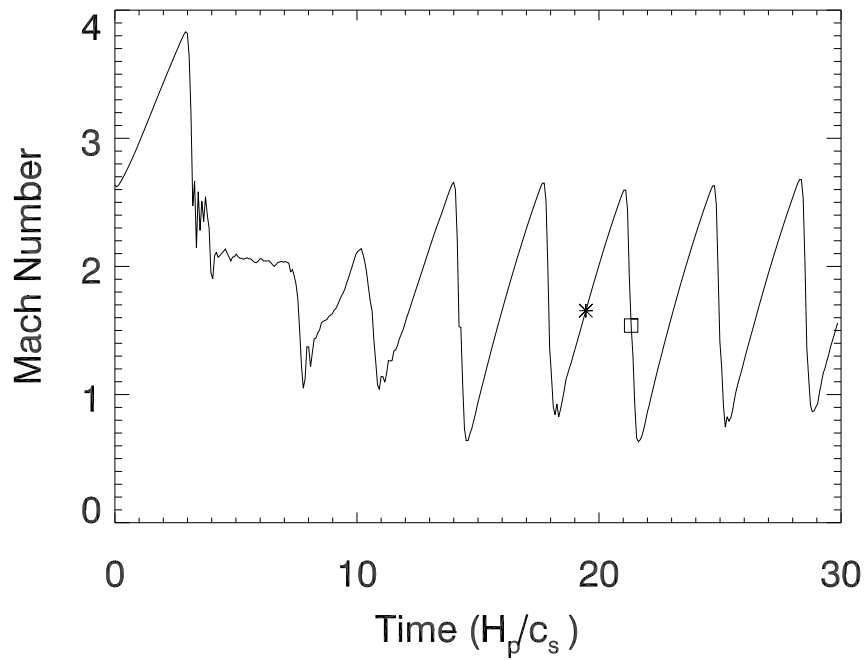


Fig. 7.— Horizontally averaged Mach number as a function of time for the slow A solution at $\chi/c_s H_p = 0.013$, $\epsilon = 0.01$. The steady state after time $\sim 10 H_p/c_s$ alternates between phases of gradual acceleration, and sharp drops of Mach number due to a violent instability. The star and box denote points at which we illustrate the vector field in figs 9 and 10.

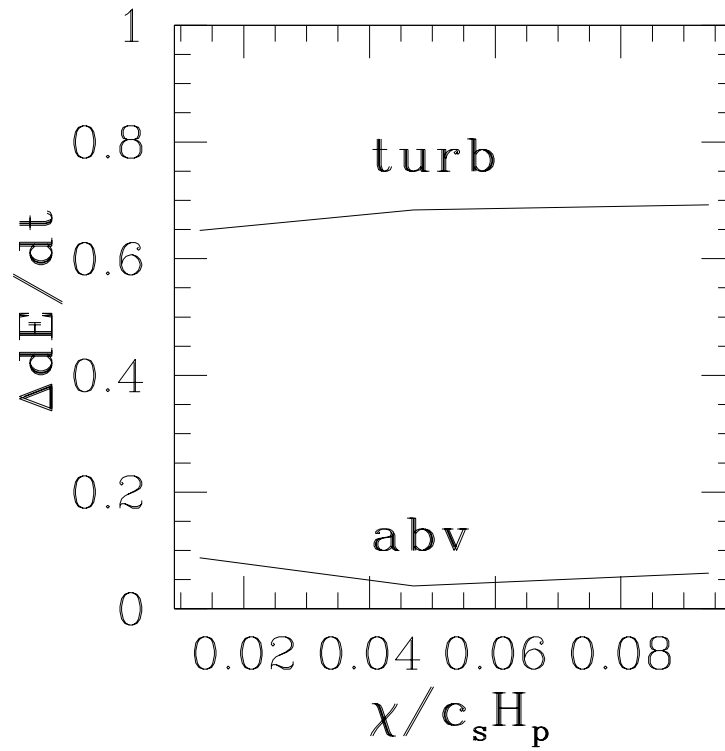


Fig. 8.— Dissipation fractions via artificial bulk viscosity (abv) and turbulence at $\epsilon = 0.01$ and the sequence of $\chi/c_s H_p$ from Table 3. The turbulent dissipation is largely irreversible compression, and it dominates over the shock dissipation.

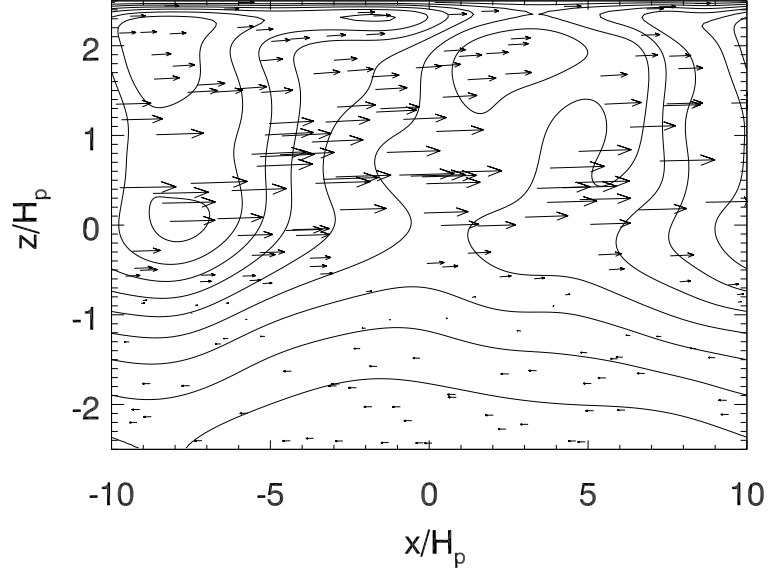


Fig. 9.— Velocity field for the slow A solution at $\chi/c_s H_p = 0.013$, $\epsilon = 0.01$ during the drive up phase (starred point in Fig. 9). Equally spaced temperature contours are overlaid from T_{wall} to $T_{\text{max}} = 1.07T_{\text{wall}}$. The minimum Richardson number is $Ri = 0.11$.

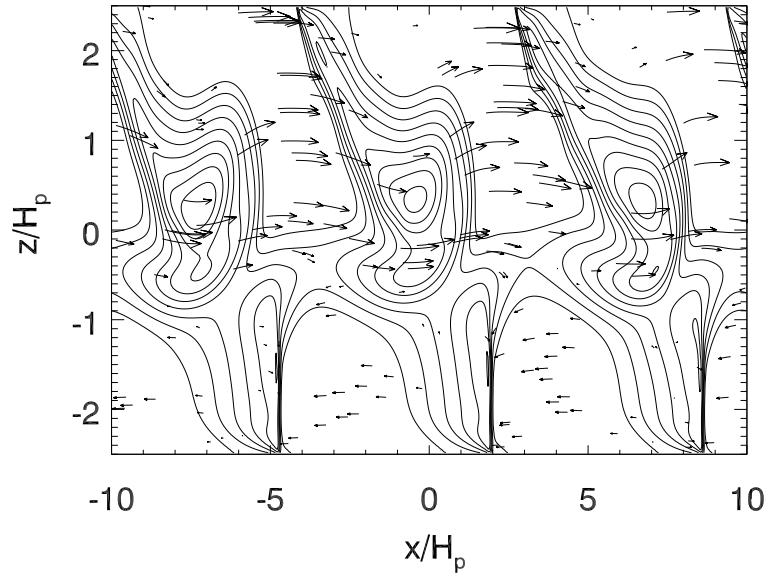


Fig. 10.— Like Fig. 9 but during the unstable phase (boxed point in Fig 9), and with contours from T_{wall} to $T_{\text{max}} = 1.46T_{\text{wall}}$. Minimum $Ri = 0.04$. Periodic shocks occur at $z/H_p < -1$, but the bulk of the heating is due to irreversible compression.

represent horizontal shears (which we do not) and hydraulic jumps (e.g Showman et al. 2009; Rauscher & Menou 2009), which bear some resemblance to shocks but do not conserve energy and may not be triggered in the same circumstances. Therefore no particular reason exists as to why our results for the wind speeds should agree quantitatively with those obtained from the primitive equations, for example.

Comparison with the calculations carried out by Burkert et al. (2005), Dobbs-Dixon & Lin (2008) and Dobbs-Dixon et al. (2010, hereafter DCL) is potentially more revealing, because these calculations, like ours, use the full compressible hydrodynamic equations. The most recent of these studies included an explicit shear viscosity. It was found that the viscosity had little effect unless at least $10^{10} \text{ cm}^2 \text{ s}^{-1}$, above which the speed decreased monotonically. For reference, $\nu = 10^{10} \text{ cm}^2 \text{ s}^{-1}$ corresponds to $Re \approx 600$ referred to the sound speed and scale height. We find, however, that the wind speed is not monotonic or even single-valued in the viscosity (Fig. (4)).

We would like to understand what accounts for the difference between our results and those of DCL. Compared to our body force and constant diffusivity, the thermal forcing and radiative transfer implemented by DCL is much more sophisticated and realistic, but it is hard to see what this has to do with the viscous effects, especially since the behavior seen in Fig. (4) exists for all choices of forcing and diffusivity that we have tried. Furthermore, our direct forcing is usually stronger than DCL’s thermal forcing since, for example, a horizontal acceleration of $f = 0.025 g$ would result in a Mach number $\sqrt{2\pi R_p f}/c_s \gtrsim 7$ after going half way around the planet without dissipation. And yet our Mach numbers are at most comparable to those of DCL, the latter peaking at ~ 3 for low viscosity.

More likely the difference in results has to do either with the difference in the dimensionality and geometry of the calculations (3D and global for DCL; 2D and local for us), or with spatial resolution. It is well known that subsonic turbulence behaves differently in two and three dimensions; however, since two dimensions usually favor energy on large scales, our wind speeds might have been expected to exceed DCL’s if dimensionality were the most important factor. Concerning numerical resolution, it appears that DCL’s standard value is $\lesssim 4$ cells per scale height, compared to our 10. Since we and DCL use similar numerical methods, their calculations are probably more diffusive than ours. When we use a resolution comparable to theirs, our wind speeds actually increase for the same forcing (§4.4). The fact that we and they find comparable Mach numbers at our highest respective Reynolds numbers suggests that our stronger forcing is partly offset by our finer resolution.

A limitation of our local, two-dimensional models is the somewhat arbitrary assumption that the nonpotential horizontal force is compensated over a depth range $\Delta z \approx 2H_p$. Other things being equal, one would expect the flow speed to scale as $(\Delta z)^{1/2}$ at constant forcing

amplitude if Richardson number rather than Mach number is the controlling parameter. Inspection of DCL’s figures suggests that the horizontal speed scales approximately linearly in $\ln p$ over the range 10^{-4} - 10^0 bar. The sign change is not always obvious in their velocity plots, although they infer the existence of return flow from their temperature profiles. However, since the momentum density $\rho \bar{v}_x \propto v_x(z) \exp(-z/H_p)$, this is much better localized around its sign change than is v_x itself.

We can use our turbulent viscosities to estimate a turbulent diffusivity for composition, K_t , as may be required to keep the upper atmosphere turbulently mixed (Spiegel et al. 2009). The Schmidt number, defined by $Sc_t = \nu_t/K_t$, in general has a complicated dependence on flow properties (see e.g., Huq & Stewart 2008). For $Ri \lesssim O(10^{-1})$, however, Sc_t is independent of Ri and of order unity. The data in Table 4 then gives us mass diffusivities pertaining to the shear layers in Hot Jupiter atmospheres: $K_t \gtrsim 10^{-3}c_s H_p \sim 10^{10} \text{ cm}^2 \text{ s}^{-1}$. Spiegel et al. (2009) estimated that $K_t \sim 10^7 - 10^{11} \text{ cm}^2 \text{ s}^{-1}$ is required, depending on grain size, to maintain TiO as an optical absorber at $p \lesssim 1$ mbar. Our values are toward the upper end of this range, but only in the shear layer ($\sim 2H_p$). To estimate K_t elsewhere, we would need to estimate how much of the mechanical power dissipated in the shear layer can propagate upwards and downwards in the form of internal waves or shocks. This we have not attempted.

6. Conclusions

We have investigated the balance between horizontal forcing and mechanical dissipation in model shear flows designed to imitate thermally driven winds of jovian exoplanets. Our main conclusions are as follows.

1. Following Paper I, some form of mechanical dissipation is required to offset the production of mechanical energy by the longitudinal entropy gradient. Plausible dissipation mechanisms include shocks, turbulence, and MHD drag.
2. Entropy stratification has a stabilizing influence on Kelvin-Helmholtz (KH) modes, but thermal diffusivity (χ) tends to undercut this influence to a degree that can be quantified by the Peclet number $Pe \equiv c_s H_p / \chi$ based on the sound speed (c_s) and pressure scale height (H_p). We estimate $Pe \sim O(10^3)$ at the altitude where the thermal timescale is comparable to the circumferential flow time at Mach 1, but $Pe \lesssim O(1)$ near the infrared photosphere.
3. Linear analysis indicates that for $Pe \gtrsim 10$, thermal diffusion has little effect on the stability of KH modes whose horizontal wavelength is comparable to the vertical thickness

of the shear layer; the usual adiabatic Richardson criterion $Ri \equiv N^2/(\partial U/\partial z)^2 > 1/4$ is sufficient for the stability of these short-wavelength modes. For typical conditions on the day sides of hot Jupiters, $Ri < 1/4$ implies transsonic or supersonic winds, presuming that the shear layer is no narrower than a pressure scale height.

4. Nevertheless, at any finite Pe and Ri , inviscid flows with an inflection point in the shear profile are unstable at sufficiently long horizontal wavelengths, at least when the flow is confined within a channel of finite vertical extent. We doubt that these long-wavelength KH modes are important for hot-Jupiter winds because their growth rates are very small (inversely proportional to wavelength) and because the planetary circumference is not large enough compared to H_p to accommodate them at $Pe \gtrsim 10^3$.
5. We estimate a turbulent diffusivity for composition in hot Jupiter atmospheres. For $Pe \approx 100$, we find $K_t/c_s H_p \approx 10^{-3}$, depending on the strength of the horizontal forcing. However, these values pertain to regions of maximum vertical shear; turbulent diffusivities may be much smaller elsewhere.
6. Nonlinear, two-dimensional (azimuth and depth), horizontally forced local simulations saturate at time-averaged Mach numbers ~ 2 when the Reynolds number $Re \equiv c_s H_p/\nu \gtrsim 10^3$. Given the widths of our shear layers ($\sim 2H_p$) and background stratification, this corresponds to minimum Richardson numbers slightly below the adiabatic critical value of $1/4$. In this regime, which is relevant to hot Jupiters, we find that the saturated wind speed depends only weakly on Pe and on the strength of the forcing.
7. Dissipation in the high- Re regime is due mainly to the work expended to overturn the stratification rather than shocks, though weak shocks are present. It is highly intermittent, at least in our two-dimensional calculations, and appears to be triggered by a recurrent linear instability of Kelvin-Helmholtz type.
8. At $Re \lesssim 10^3$ or at low numerical resolution (significantly fewer than 10 cells per pressure scale height), multiple sequences of solutions appear in overlapping ranges of Reynolds number, differing in their wind speed and predominant dissipation mechanisms. The fastest have Mach numbers at least twice as large as what we believe to be the correct inviscid values for our forcing strengths.

The last three points suggest that some global simulations of hot Jupiters may have overestimated wind speeds due to incomplete physics (e.g. neglect of vertical accelerations and sound waves) and/or insufficient spatial resolution. Pending sufficient computational resources to resolve the physical dissipation mechanisms directly in global simulations, we suggest that artificial dissipative terms be added to the equations of motion so as to prevent

strongly supersonic shears and small Richardson numbers. The appropriate form for these terms will depend upon the equation sets and algorithms used, but presumably it is desirable that they conserve energy and momentum, and probably that they have a sharp threshold in Mach number or Richardson number.

We thank Jim Stone for help with ZEUS. This work was supported in part by the National Science foundation under grant AST-0707373.

REFERENCES

- Arras, P. & Socrates, A. 2010, *ApJ*, 714, 1
- Batygin, K. & Stevenson, D. J. 2010, *ApJ*, 714, L238
- Burkert, A., Lin, D. N. C., Bodenheimer, P. H., Jones, C. A., & Yorke, H. W. 2005, *ApJ*, 618, 512
- Chandrasekhar, S. 1961, *Hydrodynamic and hydromagnetic stability* (Oxford: Oxford University Press)
- Cooper, C. S. & Showman, A. P. 2005, *ApJ*, 629, L45
- Dobbs-Dixon, I., Cumming, A., & Lin, D. N. C. 2010, *ApJ*, 710, 1395
- Dobbs-Dixon, I. & Lin, D. N. C. 2008, *ApJ*, 673, 513
- Drazin, P. G. & Reid, W. H. 1981, *Hydrodynamic Stability* (Cambridge: Cambridge University Press)
- Dudis, J. J. 1973, *J. Fluid Mech.*, 58, 81
- . 1974, *J. Fluid Mech.*, 64, 65
- Fricke, K. 1968, *Zeitschrift für Astrophysik*, 317
- Gage, K. S. 1972, *Phys. Fluids*, 15, 526
- . 1973, *Bound.-Layer Meteorology*, 5, 3
- Goldreich, P. & Schubert, G. 1967, *ApJ*, 150, 571
- Goodman, J. 2009, *ApJ*, 693, 1645, (Paper I)

- Guillot, T. & Showman, A. P. 2002, *A&A*, 385, 156
- Huq, P. & Stewart, E. J. 2008, *Geophys. Res. Lett.*, 35, L23604
- Koppel, D. 1964, *J. Math. Phys.*, 5, 963
- Maslowe, S. A. & Thompson, J. M. 1971, *Phys. Fluids*, 14, 453
- Miller, J. J. & Gage, K. S. 1972, *Phys. Fluids*, 15, 723
- Perna, R., Menou, K., & Rauscher, E. 2010, ArXiv e-prints
- Rauscher, E. & Menou, K. 2009, ArXiv e-prints
- Showman, A. P., Fortney, J. J., Lian, Y., Marley, M. S., Freedman, R. S., Knutson, H. A., & Charbonneau, D. 2009, *ApJ*, 699, 564
- Spiegel, D. S., Silverio, K., & Burrows, A. 2009, *ApJ*, 699, 1487
- Stiel, L. I. & Thodos, G. 1963, *Industrial & Engineering Chemistry Fundamentals*, 2, 233
- Stone, J. M. & Norman, M. L. 1992, *ApJ*, 80, 753

A. Exact linear solutions

We provide here four limits of eqns 14a and 14b for which there analytic solutions. We test our code against these solutions.

Taking $N^2 = 0, \nu \rightarrow 0$, eqns 14a and 14b admit solutions satisfying the inviscid perturbation equation with vanishing temperature perturbation,

$$v''_{1z} = \left(-\frac{k_x U''}{\sigma} + k^2 \right) v_{1z}, \quad (\text{A1})$$

$$\theta_1 = 0, \quad (\text{A2})$$

in which $k \equiv (k_x^2 + k_y^2)^{1/2}$. For a hyperbolic tangent velocity profile $U = \tanh(z)$, the inviscid perturbation equation for the marginal $\omega = 0$ mode becomes

$$v''_{1z} = - (2\text{sech}^2 z - k^2) v_{1z}. \quad (\text{A3})$$

A solution to this equation that vanishes as $z \rightarrow \pm\infty$ is

$$v_{1z} = \text{sech} z, \quad k^2 = 1. \quad (\text{A4})$$

In the limit

$$U = 0, \nu \rightarrow 0, N^2 = 0, \quad (\text{A5})$$

eqns 14a and 14b become

$$v''_{1z} = (k^2)v_{1z} - \frac{i}{\omega}k^2\theta_1, \quad (\text{A6})$$

$$\theta''_1 = \left(-\frac{i\omega}{\chi} + k^2 \right) \theta_1, \quad (\text{A7})$$

which for $Re(\omega) = 0$ and $Im(\omega) < -(k^2)\chi$ admit the decaying mode solutions

$$\theta_1 = A \cos \left[\left(-k^2 + \frac{i\omega}{\chi} \right)^{1/2} z + \phi \right], \quad (\text{A8})$$

$$v_{1z} = A \frac{\chi k^2}{\omega^2} \cos \left[\left(-k^2 + \frac{i\omega}{\chi} \right)^{1/2} z + \phi \right] + B e^{kz} + C e^{-kz}. \quad (\text{A9})$$

In the limit $\chi \rightarrow \infty$ with conditions A5, we obtain solutions to eqns A6 and A7 of the form

$$\theta_1 = A e^{kz} + B e^{-kz}, \quad (\text{A10})$$

$$v_{1z} = \frac{i}{4\omega} (Ae^{kz} + Be^{-kz} + 2kz (Ae^{kz} - Be^{-kz})) + Ce^{kz} + De^{-kz}. \quad (\text{A11})$$

Finally, in the limit

$$U = 0, \chi \rightarrow 0, \nu \rightarrow 0, \quad (\text{A12})$$

eqns 14a and 14b combine to give

$$v_{1z}'' = k^2 \left(1 - \frac{N^2}{\omega^2}\right) v_{1z}. \quad (\text{A13})$$

For ω real and $N^2/\omega^2 > 1$, eqn A13 has solutions of the form

$$v_{1z} = A \cos \left[k \left(\frac{N^2}{\omega^2} - 1 \right)^{1/2} z + \phi \right], \quad (\text{A14})$$

$$\theta_1 = A \frac{iN^2}{\omega} \cos \left[k \left(\frac{N^2}{\omega^2} - 1 \right)^{1/2} z + \phi \right]. \quad (\text{A15})$$

B. Long-wavelength modes

Here we demonstrate analytically for the Boussinesq equations that there exist long-wavelength instabilities at arbitrarily large Richardson number if the Peclet number is finite. It is helpful to adopt dimensionless variables. Supposing $U(z) \approx \pm U_0$ at $|z| \gg H$, where H is the width of the shear layer, we define these variables as follows:

$$\begin{aligned} z_* &= z/H & U_*(z_*) &= U(z)/U_0 \\ v_*(z_*) &= v_{1z}(z)/U_0 & \theta_* &= \frac{\theta_1}{N^2 H} \\ k_* &= H \sqrt{k_x^2 + k_y^2} & \cos \alpha &= k_x / \sqrt{k_x^2 + k_y^2} & c_* &= \omega / (k_x U_0) \\ Re &= U_0 H / \nu & Pe &= U_0 H / \chi & Ri &= (NH/U_0)^2. \end{aligned} \quad (\text{B1})$$

Equations (14a) & (14b) become, with primes denoting d/dz_* ,

$$\left[v_*'' + \frac{U_*''}{c_* - U_*} v_* - k_*^2 v_* \right] (c_* - U_*) \cos \alpha - \frac{i}{k_* Re} \left(\frac{d^2}{dz_*^2} - k_*^2 \right)^2 v_* = -Ri k_* \theta_*, \quad (\text{B2a})$$

$$\theta_*'' + [iPe k_* \cos \alpha (c_* - U_*) - k_*^2] \theta_* = Pe v_*. \quad (\text{B2b})$$

We take the inviscid, long wavelength limit in such a way that $k_* Re \rightarrow \infty$ while $k_* \rightarrow 0^+$, with Pe and Ri regarded as finite and nonzero. The wavelength $2\pi/|\mathbf{k}|^{-1}$ is not infinite, but

rather $\gg 2\pi H$, so that we may neglect the explicit appearances of k_* in the equations above yet regard c_* as finite. If c_* should turn out to have an imaginary part, then the growth rate $\text{Im}(\omega) \rightarrow k_x U_0 \text{Im}(c_*)$ as $k_* \rightarrow 0$. The potential temperature θ_* decouples:

$$v_*'' + \frac{U_*''}{c_* - U_*} v_* = 0, \quad (\text{B3a})$$

$$\theta_*'' = Pe v_*. \quad (\text{B3b})$$

The first of equations (B3) is the long-wavelength limit of the inviscid, unstratified Kelvin-Helmholtz problem with a continuous shear profile $U_*(z_*)$. Given boundary conditions $v_*(\pm z_{*,\text{max}}) = 0$ for some $z_{*,\text{max}}$ that is finite and sufficiently large, and presuming that U_* is an odd function of z_* so that $U_*''(0) = 0$, then there is a solution to (B3) for which c_* has a positive imaginary part. In fact, although it doesn't satisfy the boundary conditions, $v_* \propto U_* - c_*$ is a solution to eq. (B3a) for any c_* , and a second solution $v_* = f(z_*)(U_* - c_*)$ can be found by solving a first-order equation for $f'(z_*)$, followed by a quadrature. Requiring that this solution vanish at both $\pm z_{*,\text{max}}$ determines c_* via

$$\int_{-z_{*,\text{max}}}^{z_{*,\text{max}}} \frac{dz_*}{[U_*(z_*) - c_*]^2} = 0. \quad (\text{B4})$$

Since U_* is odd and $\approx \pm 1$ at large $|z_*|$, it follows easily that $c_* \approx \pm i$ when $z_{*,\text{max}} \gg 1$.

This demonstrates the existence of inviscid instability when $|\mathbf{k}|^{-1} \gg z_{*,\text{max}}^2 \gg 1$. If $z_{*,\text{max}} \gtrsim k_*^{-1/2}$, however, then a separate analysis would be needed, because the solution of eq. (B3b) might yield $\theta_* \sim Pe z_{*,\text{max}}^2 v_*$, and then the righthand side of eq. (B2a) could be $O(1)$ or larger. We have not done this analysis because the numerical evidence indicates that the long-wavelength growth rates are too slow to be important for our applications.